Traffic-induced multicomponent ultrafine particle microphysics in the WRF v3.6.1 large eddy simulation model

Zhong, Jian; Nikolova, Irina; Cai, Xiaoming; MacKenzie, A. Robert; Alam, Salim; Xu, Ruixin; Singh, Ajit; Harrison, Roy

DOI:
10.1016/j.atmosenv.2019.117213

Traffic-induced multicomponent ultrafine particle microphysics in the WRF v3.6.1 large eddy simulation model: General behaviour from idealised scenarios at the neighbourhood-scale

Jian Zhong[1], Irina Nikolova[1], Xiaoming Cai[1*], A. Rob MacKenzie[1,2], Mohammed S. Alam[1], Ruixin Xu[1], Ajit Singh[1] and Roy M. Harrison[1,†]

[1]School of Geography, Earth & Environmental Sciences
University of Birmingham
Edgbaston, Birmingham, B15 2TT
United Kingdom

[2]Birmingham Institute of Forest Research
University of Birmingham
Edgbaston, Birmingham, B15 2TT
United Kingdom

[*] **Corresponding Author**: Xiaoming Cai (x.cai@bham.ac.uk)

[†] **Also at**: Department of Environmental Sciences / Center of Excellence in Environmental Studies, King Abdulaziz University, PO Box 80203, Jeddah, 21589, Saudi Arabia

HIGHLIGHTS

1) Multicomponent microphysics of UFPs is coupled with the WRF-LES model.

2) General behaviour of UFPs on the neighbourhood scale dispersion is investigated.

3) The combined effects of emissions, mixing and microphysics of UFPs are revealed.

ABSTRACT

Traffic is the key source of ultrafine particles (UFPs, particulate matter with an aerodynamic diameter less than 0.1 μm or 100 nm) in most urban areas. The traffic-generated UFPs vented out from an urban street mix with overlying 'urban background air' and are diluted whilst also undergoing change due to condensation/evaporation and other aerosol microphysics. Traffic-generated UFPs are comprised of a complex mixture of semi-volatile compounds (SVOCs) with volatility varying over many orders of magnitude, resulting in size-dependent particle composition. This study coupled the multicomponent microphysics (involving condensation/evaporation) of UFPs with the WRF v3.6.1 (Weather Research and Forecasting) large eddy simulation model (i.e. WRF-LES-UFP), and used this modelling system to investigate the general behaviour of UFPs on the neighbourhood scale (10-1,000 m; transport times of few minutes) for idealised scenarios. The model captures the horizontal dispersion of UFPs downwind into the neighbourhood scale and vertical mixing with urban background air. Evaporation decreases the mode size of UFPs venting into the urban boundary layer from street-level. The neighbourhood-scale evolution of UFPs is, therefore, a combination of the effects of emissions, mixing with background, and condensation/evaporation. Total UFP number concentration and total mass concentrations scale linearly with the emission rate or the background concentration, demonstrating numerical conservation of the scheme. The linearity is less pronounced for the number concentration of smaller particles (UFP diameter less than 100 nm) with respect to UFP size and concentrations of those carbon components with a time scale comparable to the dilution time scale (in the order of minutes), reflecting the effects (altering the particle sizes) due to condensation/evaporation.

Keywords: Atmospheric nanoparticles; Urban pollution; Aerosol microphysics; Urban Street; Semi-volatiles.

1. INTRODUCTION

Ultrafine particles (UFPs or $PM_{0.1}$, particulate matter with an aerodynamic diameter $D_p < 0.1$ μm) are respirable (Manigrasso et al., 2017) and may cause adverse health effects to the pulmonary system, and the cardiovascular/nervous systems (e.g. Panis et al., 2010; Geiser et al., 2005). Unlike larger size fractions PM_{10} ($D_p < 10$ μm) and $PM_{2.5}$ ($D_p < 2.5$ μm) (US EPA, 2017; European Commission, 2017), there are currently no ambient air quality regulations for UFPs. UFPs dominate particle size number concentrations (Harrison et al., 2000) and have received increasing attention from the scientific community (e.g. Dall'Osto et al., 2011; Harrison et al., 2011; Vu et al., 2017; Jacobson et al., 2005). UFPs from vehicle emissions, which tend to dominate the urban atmosphere (Harrison et al., 2018; Kumar et al., 2014), contain multi-components of semi-volatile compounds (SVOCs) (Alam et al., 2016; Baldauf et al., 2016), contributing to the changes in particle size due to condensation/evaporation (Harrison et al., 2016; Jacobson et al., 2005).

Condensation and evaporation are among the most important aerosol microphysical processes in predicting the fate of ultrafine particles in urban air (Gelbard and Seinfeld, 1980; Harrison et al., 2016; Jacobson, 2005; Jacobson and Turco, 1995; Jacobson et al., 1996; Pankow, 1994). Nikolova et al. (2016) developed a CiTTy-Street-UFP box model, an urban version of CiTTyCAT Lagrangian model (Pugh et al., 2012) including aerosol microphysics. The model was used to assess the importance of microphysical processes and to simulate the behaviour of traffic-related UFPs within a street canyon and UFP evolution from canyon rooftop to a nearby downwind urban park. For a steady-state simulation of number concentration in the canyon, there is a balance among the traffic-related UFP emissions, aerosol microphysics, and exchange with the rooftop air. There is also evidence of the evaporation of UFPs when the rooftop air is advected to the neighbourhood park. Nikolova et al. (2018) further used this box model approach to investigate the influence of particle composition on the evolution of particle size distributions at the time scale of 100s (related to the dispersion at the neighbourhood scale). The evaporative shrinkage of UFPs from the nucleation mode

was highly influenced by SVOC composition. Zhong et al. (2018) coupled the UFP multicomponent microphysics (i.e. evaporation/condensation of SVOCs) with a two-box model for urban street canyon compartments and investigated factors that may inhibit mixing. The contrasts in the UFP number-size distribution between the lower and upper canyons are captured by this two-box-UFP canyon model. The traditional assumption of a one box model for a compartmentalised canyon would typically under-predict the UFP number concentration in the lower canyon compared with the proposed two-box model. The traffic-generated nanoparticles vented out from an urban street network, which may be simulated by a street canyon box model (Nikolova et al., 2016), could be evaporated to smaller particles while they are transported during neighbourhood scale dispersion (Dall'Osto et al., 2011; Harrison et al., 2019).

According to the horizontal length scale, Britter and Hanna (2003) classified the atmospheric flow and related phenomena (e.g. dispersion of pollutants) into four categories: i.e. regional scale (~100-200 km), urban/city scale (~10-20 km), neighbourhood scale (~1-2 km) and local/street scale (~0.1-0.2 km). The neighbourhood scale has been increasingly concentrated on by the urban research community. This is a scale over which the computation can be feasible at high spatial and temporal resolution (Carpentieri et al., 2012).

The large-eddy simulation (LES) mode of the Weather Research and Forecasting (WRF) model (WRF-LES) (Skamarock and Klemp, 2008) is a powerful tool to simulate the turbulence-resolved atmospheric flow at the neighbourhood scale in 3-dimensional (3D) Eulerian grids with high spatial and temporal resolutions. Nottrott et al. (2014) investigated the dispersion of a passive scalar from continuous point sources within the atmospheric boundary layer using the WRF-LES. The plume trajectories were captured by the model. Nunalee et al. (2014) also simulated the plume impingement of a passive scalar in the atmospheric turbulent flow influenced by complex terrain features. The spatial pattern of the surface plume trajectory was well revealed by the WRF-LES. Jacobson and

Seinfeld (2004) investigated the dispersion and the evolution of soot particle size distributions from both point and line sources using a 3D global-through-urban atmospheric model. There was a reduction in the particle number concentrations downwind of the emission sources, primarily due to dilution. The WRF-CHEM mesoscale model (Grell et al., 2005) provides the capability of coupling WRF with "online" chemistry involving several aerosol schemes, such as GOCART (From the Goddard Chemistry Aerosol Radiation and Transport model) (Chin et al., 2000), MOSAIC (Model for Simulating Aerosol Interactions and Chemistry) (Zaveri et al., 2008) and MADE/SORGAM (The Modal Aerosol Dynamics Model for Europe with secondary organic aerosols) (Ackermann et al., 1998; Schell et al., 2001). However, there is no aerosol size information for GOCART, only 4 or 8 size bins up to PM_{10} for MOSAIC and 3 log-normal aerosol modes (i.e. Aitken, accumulation and coarse) for MADE/SORGAM. There are currently no prior studies using WRF-LES at the neighbourhood/micro scale and multicomponent aerosol microphysics for UFPs at the nanoparticle scale.

In this study, the multicomponent microphysics (i.e. condensation/evaporation) of UFPs is coupled with WRF-LES (WRF-LES-UFP) to simulate the evolution and dispersion of UFPs at the neighbourhood scale for idealised scenarios of road emissions. The UFP code was previously implemented into CiTTy-Street-UFP (Nikolova et al., 2016) and the compartmentalised canyon box model (Zhong et al., 2018). Condensation and evaporation in the presence of semi-volatiles are processes that can actively re-partition semi-volatiles between gas and particle, alter the sizes of the UFPs and change the chemical composition of UFPs. With the proposed model (WRF-LES-UFP), we can explore a very complex system of interactions between particles, emissions, atmosphere and mixing, and quantify those interactions.

2. METHODS

2.1 The WRF-LES Model

The WRF-LES model explicitly calculates the larger resolved eddies with the smaller unresolved eddies parameterised by subgrid-scale (SGS) turbulence models (Moeng et al., 2007) and can be used for the neighbourhood scale simulation. LES simulations, therefore, allow for intermittency in turbulence in a way that cannot be captured by Reynolds-average Navier-Stokes (RANS) (e.g. Solazzo et al., 2008; Baik et al., 2007; Kwak and Baik, 2014) or semi-analytical Gaussian dispersion methods (e.g. McHugh et al., 1997; Popoola et al., 2018; Munir and Habeebullah, 2018). The filtered continuity and Navier-Stokes equations can be described as follows (Munoz-Esparza et al., 2015):

$$\frac{\partial \tilde{u}_i}{\partial x_i} = 0, \quad (1)$$

$$\frac{\partial \tilde{u}_i}{\partial t} + \frac{\partial \tilde{u}_i \tilde{u}_j}{\partial x_j} = \upsilon \frac{\partial^2 \tilde{u}_i}{\partial x_j \partial x_j} - \frac{1}{\tilde{\rho}} \frac{\partial \tilde{p}}{\partial x_i} - \frac{\partial \tau_{ij}}{\partial x_j} + f_c \epsilon_{ij3} \left(\tilde{u}_j - U_{g,j} \right), \quad (2)$$

where $\tilde{u}_i$ represents the i^{th} component of resolved velocity with i (or j) =1, 2, 3 indicating x, y, z directions; x_i (or x_j) denotes the i^{th} (or j^{th}) component of spatial coordinates; t is time; $\tilde{p}$ is the resolved pressure; $\tilde{\rho}$ is the resolved density; f_c denotes the Coriolis parameter due to the rotation of Earth (here, $f_c = 1.139 \times 10^{-4} s^{-1}$, representing a latitude of 51.526 N); ϵ_{ij3} denotes the alternating unit tensor; $U_{g,j}$ denotes the geostrophic wind; υ is the kinematic molecular viscosity; τ_{ij} denotes the SGS stress tensor, which is parameterised by the 1.5-order turbulent kinetic energy (TKE) SGS model (See Section A in the Supplementary Material for details).

2.2 Size-Dependent Multicomponent Microphysics of UFPs

The multicomponent microphysics of UFPs considered in the current WRF-LES model include the condensation and evaporation processes of SVOCs, which are the dominant microphysical processes in predicting the neighbourhood scale evolution of UFPs in urban air (Nikolova et al., 2016). For the purpose of this study, coagulation and deposition processes have been omitted as these play a far lesser role than evaporation processes on the short timescales of neighbourhood atmospheric transport

(Nikolova et al., 2016). Nikolova et al. (2016) suggested that the exclusion of coagulation (with a coagulation kernel accounting for Brownian motion) and deposition processes in the street canyon model would lead to a reduction of the total particle number by 4.7% - 8.2% depending on the ventilation conditions. Jacobson et al. (2005) suggested that Brownian motion together with van der Waals/viscous forces and fractal geometry were the three most important processes in the treatment of coagulation kernel and it was essential to consider both evaporation and coagulation in the model for nanoparticles below 15 nm near a roadway, especially when there was a peak diameter less than 10 nm for the nucleation mode. In this current modelling study, we focus on the relative importance of the processes, i.e. mixing vs. condensation and evaporation processes, emission vs. background. By using the sectional modelling approach, the mass transfer rate between particulate and gas phases due to the condensation and evaporation processes for the *q*-th component SVOC of one particle in the *jb*-th size bin can be estimated as follows (Jacobson, 2005):

$$\frac{d\tilde{m}_{q,jb}}{dt} = a_{FS}^{jb} \frac{2\pi D_{p,jb} M_q D_q}{RT} (e_q^{\infty} - X_{q,jb} a_K^{q,jb} e_q^{vap}), \quad (3)$$

where *q* is for the *q*-th component; *jb* is for *jb*-th size bin; a_{FS} is the Fuchs-Sutugin correction factor; D_p represents the particle diameter (m); *M* is the molar mass (g mol^{-1}); D_q denotes the vapour diffusivity (m^2 s^{-1}); R is the universal gas constant (J mol^{-1} K^{-1}); T is the temperature (K); e_q^{∞} is the partial pressure in the ambient air (Pa); *X* is the molar fraction; a_K accounts for the Kelvin effect; e_q^{vap} is the saturation vapour pressure (Pa), i.e. the vapour pressure of the chemical species evaporating from the particle surfaces. e_q^{∞} is derived from the gas-phase concentration of component *q* based on the ideal gas law, while e_q^{vap} is based on the method of (Compernolle et al., 2011) found in the UManSysProp online tool (Topping et al., 2016). The saturation vapour pressure using the method of Compernolle et al. (2011) was tested and compared with other vapour pressure estimation methods in Nikolova et al. (2018) and informed by measurements of vapour pressure made in our laboratory (Alam et al., 2019).

Table 1 shows the initial partial pressure at the inlet of the model and the saturation vapour pressure estimated at temperature of 284.15 K based on the UManSysProp online tool using data from Compernolle et al. (2011). When $\frac{d\tilde{m}_{q,jb}}{dt} > 0$ in Equation 3, vapour condenses on the particles; when $\frac{d\tilde{m}_{q,jb}}{dt} < 0$ in Equation 3, evaporation of SVOCs from the particle phase takes place. The overall production of gaseous component *q* due to multicomponent microphysics of UFPs can be calculated as:

$$\Delta\tilde{c}_q = -\sum_{jb} \frac{\tilde{N}_{jb} d\tilde{m}_{q,jb}}{dt}, \quad (4)$$

where $\tilde{N}_{jb}$ is the number concentration for the *jb*-th size bin. A dynamical size (d_{jn}) is calculated for each size bin after the condensation and evaporation processes and a redistribution scheme is implemented to redistribute both UFP number and mass concentrations to the sectional bin (See Section B in the Supplementary Material for details).

The UFP composition in our default UFP module configuration includes 18 components, i.e. 1 non-volatile core and 17 surrogate n-alkane components (SVOCs), i.e. $C_{16}H_{34}$-$C_{32}H_{66}$ (labelled 'C16' – 'C32', below). The hundreds of SVOC components found in UFP (Alam et al., 2016) are mapped onto these surrogates on the basis of their volatility (Nikolova et al., 2018) (See Table S1 in the Supplementary Material for the volatility bin information, grouped n-alkane/surrogate n-alkane used in this study). These volatility classes are derived based on the GC × GC chromatogram with the same carbon numbers in different carbon arrangements (e.g. straight-chain or branched-chain) (Alam et al., 2016). Particle size is sectioned into 15 equally-sized bins on a logarithmic scale, covering particles with geometric mean diameter of 6.7 nm – 501.4 nm. There are 17 SVOC components in the gas-phase, corresponding to each surrogate n-alkane. The UFP number concentration of each size bin is updated diagnostically based on the total mass concentration of the size bin.

2.3 Framework of WRF-LES-UFP Coupling

The dispersion of tracers (for both multicomponent particulate and gas phases) in the WRF-LES model is described as follows. For the multicomponent particulate phase:

$$\frac{\partial \tilde{Q}_{q,jb}}{\partial t} + \frac{\partial}{\partial x_j}\left(\tilde{Q}_{q,jb}\tilde{u}_j\right) = \frac{\partial}{\partial x_j}\left(K_c \frac{\partial \tilde{Q}_{q,jb}}{\partial x_j}\right) + \Delta\tilde{Q}_{q,jb} + E_{q,jb}, \quad (5)$$

where $\tilde{Q}$ represents the resolved UFP mass concentration; "$_q$" denotes the q-th component; "$_{jb}$" denotes the jb-th size bin; K_c is the SGS eddy diffusivity; $\Delta\tilde{Q}$ and $E_{q,jb}$ represent the resolved source terms due to multicomponent microphysics of UFPs (i.e. the condensation/evaporation processes included in the current study) and emissions, respectively.

For the multicomponent gas phase,

$$\frac{\partial \tilde{c}_q}{\partial t} + \frac{\partial}{\partial x_j}\left(\tilde{c}_q\tilde{u}_j\right) = \frac{\partial}{\partial x_j}\left(K_c \frac{\partial \tilde{c}_q}{\partial x_j}\right) + \Delta\tilde{c}_q + E_q, \quad (6)$$

where $\tilde{c}_q$ represents the resolved gas concentration for component q; $\Delta\tilde{c}_q$ and E_q represent its resolved source terms due to multicomponent microphysics of UFPs and emissions, respectively. The resolved source terms for both particulate and gas phases in Equations 5-6 are derived from the UFP multicomponent microphysics module (involving condensation/evaporation), as in previous canyon box models (Nikolova et al., 2016; Zhong et al., 2018; Nikolova et al., 2018).

2.4 WRF-LES-UFP Model Configuration and Scenarios

To demonstrate the capabilities of the WRF-LES-UFP model, we choose an idealised urban scenario driven by realistic environmental conditions and boundary conditions. Such an idealised scenario allows us to diagnose more readily the UFP dynamics. The WRF-LES computational domain used in this study (Figure S1 in the Supplementary Material) covered a horizontal area of 2.54 km × 2.54 km ($L_x \times L_y$) with 20 m × 20 m resolution. The vertical domain size is 1 km (L_z) with 79 stretch grids, so

the number of cells in the domain is 127 × 127 × 79. Because the length scales of the underlying building geometries and street canyons are about same as the grid resolution adopted here (20 m), it is not appropriate to resolve these structures explicitly. It is assumed that the height and roughness of the canopy vary slowly relative to the grid resolution, and a homogeneous urban canopy is used in this study. To focus on the evolution of multicomponent UFPs at the neighbourhood scale above the urban canopy (instead of building scale inside the urban canopy), we adopt a simplified approach of setting up the first vertical cell at a nominal 'rooftop level' and specifying momentum flux and heat flux at the bottom of the domain using observational data as discussed below.

A fixed time step of 0.2 s is adopted for the airflow calculation, whilst an adaptive time step is used for solving multicomponent condensation/evaporation of UFPs. Periodic lateral boundary conditions are specified for velocity components. Inlet conditions for the SVOC quantities (gas concentrations, particle number concentration size distributions, and particle SVOC mass fractions) are specified as fixed values. At the outlet, a zero-gradient condition is specified for all SVOC quantities.

Weather conditions adopted for the simulations are informed by observational data (Heathrow airport) for the 180°±25° wind sector during the London campaign (Jan-Feb 2017) (see Harrison et al. (2019) for details). The geostrophic wind is specified as U_g=5 m s^{-1} and V_g=10 m s^{-1} and in the presence of the Coriolis force, this attempts to achieve an approximate southerly wind of 2 m s^{-1} near the rooftop 'surface' at the bottom of the model domain. An upwelling surface sensible heat flux of 13 W m^{-2} (tke_heat_flux in the WRF namelist.input option) is adopted for the lower boundary condition of heat and a surface drag coefficient of 0.048 (tke_drag_coefficient in the namelist.input option) is specified for the lower boundary condition of momentum, derived from eddy-covariance measurements at the rooftop of Regent's University during the campaign.

The boundary layer height is initially ~ 500 m, specified by an initial constant vertical potential temperature of 282.15 K for the lower 475 m, capped by a strong inversion with of $\partial T/\partial z$ =0.05 K m^{-1} from 475 m to 625 m and $\partial T/\partial z$ =0.003 K m^{-1} from 625 m to the domain top. The meteorological conditions of a low sensible heat flux at the ground and a strong capping inversion lead to a nearly constant height of the boundary layer during the simulation period. A damping layer of 300 m is applied near the domain top to prevent gravity waves. WRF-LES was run without the UFP module for 8 hours as a spin-up period in order to achieve a quasi-steady flow. Then the UFP module was switched on for 30 min, sufficiently long compared with the timescale of the geostrophic wind advection across the domain which is about 4 min. The output of the last 10 min with an interval of 3 s was used for analysis.

An idealised street (represented by a line emission perpendicular to the surface wind direction) with a width of 40m is configured in the middle of the domain (Figure S1 in the Supplementary Material). The emission fluxes to the first vertical model level is based on those from vehicles directly into the street canyon. In this study, we introduce a BASE case scenario and the settings are as follows. The emission factor for total UFP number is 7.93×10^{13} particles $vehicle^{-1}$ km^{-1}, which is based on the value from Jones and Harrison (2006) with a correction factor for the year of 2017 derived from an analysis of measurement data (Harrison et al., 2019). The traffic activity is specified as 3740 vehicle $hour^{-1}$ at a heavily trafficked street (Marylebone Road) for the 180º wind sector during the campaign in London (Harrison et al., 2019).

The size distribution of emitted UFPs is comprised of three log-normal distributions with peaks at 21 nm, 29 nm and 69 nm, respectively, which are derived from the mode fitting for particle size distributions of the traffic increment, i.e. the background subtracted from Marylebone Road measurement at the 180º wind sector (Harrison et al., 2019). The mass fraction of non-volatile core

is assumed to be 1 % for the nucleation mode (Nikolova et al., 2016), gradually increasing to 90 % for the Aitken mode and 99 % for the accumulation mode. The mass fraction of SVOC compounds in the emitted UFPs is then scaled by the measured UFP composition in samples collected in Marylebone Road (Harrison et al., 2018).

The emission factors of total grouped SVOCs (from C16 to C32) are 681 μg veh^{-1} km^{-1} for the gas phase and 1714 μg veh^{-1} km^{-1} for the particle phase (See details in Table S2 in the Supplementary Material). The UFP size distribution at the inlet of the domain is based on the mode fitting of BT tower measurements (160 m above ground level) for the 180º wind sector during the campaign in London (Harrison et al., 2019), which has 3 log-normal distributions with peaks at 24 nm, 66 nm and 163 nm, respectively. The SVOC concentrations (gas and particles) at the inlet of the domain are based on the scaled Regent's Park measurements (inferred from the ratio of black carbon measured at BT tower to that measured at Regent's Park) (See Table S3 in the Supplementary Material for inlet SVOC concentrations). The inlet air parcel may be slightly adjusted by the multicomponent microphysics of UFPs to reach a quasi-equilibrium state after a certain travelling distance and we take 200 m before the emission at the bottom level of the domain (Figure S1 in the Supplementary Material) as the inflowing background in the analysis of the model output.

In order to investigate the effect of emissions, cases with changes in emissions only for both gas and particle phases are configured (i.e., multiplying by a coefficient, β=[0.5, 0.75, 1.25, 1.5], the emissions in the BASE case) and named EM0.5, EM0.75, EM1.25, and EM1.5, respectively. In order to investigate the effect of inlet background, cases with changes in inlet background only for both gas and particulate phases are configured using a coefficient α=[0.5, 0.75, 1.25, 1.5], i.e. case BG0.5, BG0.75, BG1.25, and BG1.5. We perform a linearity analysis by investigating the sensitivity to emissions and inlet background concentrations in both gas and particle phases.

3. RESULTS AND DISCUSSION

3.1 The BASE Case Output from the model

3.1.1 Total UFP number concentration

Figure 1(a) illustrates a vertical slice of the total UFP number concentration (UFPNC), which is averaged horizontally in the cross-wind direction and temporally over the final 10 min simulation; this gives an indication of cross-sectional dispersion of UFPs for the BASE case in the model. The total UFPNC is gradually diluted by a southerly wind from the street (the west-east line emission) to its northerly neighbourhood. The vertical expansion of the plume is observed as UFPs are advected downwind into the neighbourhood scale and vertically mixed with urban background air.

Similar neighbourhood dispersion behaviour was also observed by other simulations, i.e. Nottrott et al. (2014) and Nunalee et al. (2014) for the dispersion of a passive scalar from point sources and Jacobson and Seinfeld (2004) for the dispersion of soot particles from both point and line sources. The spatial pattern also indicates the neighbourhood dispersion of UFPs with a decrease of the total UFP number concentration downwind of the emission. This is consistent with classical line-source dispersion (Munir and Habeebullah, 2018; Jacobson and Seinfeld, 2004) and with the measured data which demonstrate that the UFPNCs in Marylebone Road were always much higher than those at its downwind neighbourhood rooftop site in Regent's Park (Dall'Osto et al., 2011; Harrison et al., 2019).

Figure 1(b) shows a vertical slice of the ratio of concentration fluctuation intensity to mean concentration for total UFPNC for the BASE case in the model. The concentration fluctuation intensity is defined as $C' = \sqrt{(C - C_m)^2}$, where C_m represents a spatial and temporal average defined earlier. The value of C'/C_m can be interpreted as the percentage of particle number fluctuation intensity in relation to its mean value caused by the unsteady turbulence generated within the LES simulation. The region upwind of emission is more determined by the fixed inlet conditions and

therefore has no significant concentration fluctuation. Once emissions are released, there is a plume expansion for the concentration fluctuation intensity in the downwind side of the emission line.

Figure 1(c) illustrates the total UFPNC (both mean concentrations and concentration fluctuation intensities) along a South-North line at the bottom model level (corresponding to just above rooftop height) as a further indication of neighbourhood dilution. The highest value indicates the effect of emissions from the street, which is similar to Figure 7(a) in Jacobson and Seinfeld (2004) for the point source dispersion. The total UFPNC decreases rapidly at the near-source downwind neighbourhood, gradually approaching the background levels. This is due to the expansion of plume as it traverses its neighbourhood downwind (Figure 1(a)). In general, the total UFPNC appears to behave like a passive scalar, as expected from the model's number-conserving numerics and lack of (because assumed slow (Nikolova et al., 2016; 2018)) coagulation, deposition, and gas-phase chemistry.

3.1.2 UFP number-size distribution

Figure 2(a) illustrates the spatially (west-east) and temporally (the final 10 min period) averaged UFP number-size distribution (UFPNSD), together with its fluctuation intensity (indicated by shaded areas), for several downwind locations at the bottom level of the domain (corresponds to the urban canopy above rooftop height) for the BASE case in the model. The black line in Figure 2(a) represents the inflowing background (200 m before the emission at the bottom level of the domain). The red line with circles at the top of the graph is for the UFPNSD of the south-side rooftop cell of the line emission source. For comparison of mode sizes, the red line with triangles at the bottom is for UFP emission rate; other lines are for the UFPNSD at downwind distances of 100 m and 400 m (or travelling time of about 50 s and 200 s), respectively. Within each WRF-LES time step of 0.2 s, both south-side and north-side rooftop cells at the line emission source receive a given amount of emitted pollutants (both particle and gas phases) and the execution of WRF's advection and diffusion modules

brings some fresher air advected from the upwind neighbour cells. Then the UFP module is applied to the mixed air parcel and to yield a new UFPNSD for the south-side rooftop cell, for example, as shown by the top curve in Figure 2(a). Comparison of this curve with the emission curve gives a clear indication of the direct influence of emission, e.g. by their same peak diameter values (peaked at bin 5 with bin bounds of [19.8 nm, 26.9 nm]). The small fluctuations of UFPNSD for the Aitken and accumulation modes (i.e. large size bins in Figure 2(a)) is explained by large fractions (90%-99%) of non-volatile core for this mode. An increase in the non-volatile core fraction will result in a decrease in the evaporative SVOCs (Nikolova et al., 2018).

There is a reduction in UFPNSD and fluctuations along the downwind distance in the simulation. There is also a clear shift of the peak particle size from the rooftop (peaked at bin 5 with bin bounds of [19.8 nm, 26.9 nm]) to its downwind locations of both 100m and 400 m (peaked at bin 4 with bin bounds of [14.6 nm, 19.8 nm]). This shift indicates particle evaporation during the neighbourhood dispersion of UFPs. The UFPNSD within the downwind neighbourhood is, therefore, a result of a combination of mixing and aerosol microphysics (i.e., condensation/evaporation of SVOCs). In the measurement in Harrison et al. (2019), there is also clear evidence of the shrinkage of particle sizes from the roadside (MR_OBS in Figure 2a with a peak diameter falling into bin 5 [19.8 nm, 26.9 nm] as defined in the model) to nearby downwind rooftop location (RU_OBS in Figure 2a with a peak diameter falling into bin 4 [14.6 nm, 19.8 nm] as defined in the model), with the lower diameter limits of 10 nm and 16 nm by the instruments adopted. This suggests that the current model can capture the general behaviour of particle size shrinkage mainly due to evaporation. The exclusion of coagulation process in our model may lead to an overestimation in the number concentration for particles below 15 nm, as suggested by Jacobson et al. (2005) with a peak diameter less than 10 nm for the nucleation mode. Since the nucleation mode in our model has a peak diameter higher than 15 nm, the effect of coagulation process may be reduced. As there are many complex conditions in the real world measurement that our current model is not able to fully represent, such as well-defined background

conditions, emission pattern, real meteorological conditions together with realistic landscape, complex aerosol microphysics processes and other model input assumptions, it is difficult for us to well match the exact number size distribution profile measured in the field campaign.

Figure 2(b) illustrates the dilution ratio, defined as $(C_{downwind} - C_{bg})/(C_{rooftop} - C_{bg})$, of UFP size fractions for downwind locations (rooftop+100m and rooftop+400m) for the BASE case in the model. For UFP size fractions with diameter greater than 100 nm, the dilution ratio closely follows that of a passive scalar (shown as size-independent dotted lines in Figure 2(b)). For these larger UFPs, the neighbourhood dispersion is dominated by dilution, attributable to the large fraction of non-volatile core in these particles. There are variations in dilution ratio for UFPs smaller than 100 nm, indicating that both dilution and condensation/evaporation are competing during the neighbourhood dispersion. Specifically, the number of medium-size particles (20 nm < D_p< 100 nm) is reduced more quickly than the rate for a passive scalar, whereas the number of small-size particles (D_p< 20 nm) is reduced more slowly than the rate for a passive scalar. Because of the simplicity of our idealised scenario, we can attribute this size-dependent behaviour to evaporation, which converts some medium-size particles to smaller-sized ones during the advection-dilution process.

3.1.3 SVOCs mass concentrations

Figure 3(a-c) shows SVOC mass concentrations in both gas and particle phases at the rooftop and downwind neighbourhood locations for the BASE case in the model. For low-carbon components (C16-C18) having higher saturation vapour pressures (Table 1), the emissions are dominated by the gas phase (Table S2) and their respective rooftop gas concentration increments (from the background) are due to the vapour emissions. For the carbon components of C19-C22, the mass emissions are dominated by the particle phase (Table S2). However, their rooftop particle concentration increments

(Figure 3b) are not significant, particularly for C19-C21. On the other hand, their rooftop gas concentration increments are of large values (Figure 3a). This simulation clearly indicates that the evaporation process proceeds very rapidly to generate higher gas concentrations (Figure 3a) before the dispersion process takes effect. This can also be seen from the particle mass concentrations which are very close to background levels at the rooftop although they are subject to particle emission fluxes (Figure 3(b)). For C22, its rooftop particle concentration increment is about 8 ng m^{-3} (Figure 3(b)), whereas its gas concentration increment is about 20 ng m^{-3} (Figure 3a).

For carbon components of C23 onwards, the mass emissions are still dominated by the particle phase (Table S2), but their rooftop concentration increments are gradually shifted from gas phase to particle phase. The contribution of evaporation is important during the neighbourhood dispersion process for SVOCs having evaporation timescales of SVOCs (Table S4 in the Supplementary Material) comparable to the dilution time scale (i.e. for C21-C26) (Nikolova et al., 2018). This is indicated by the gas concentrations, especially for C24-C26, not decreasing appreciably during the neighbourhood dispersion.

For higher carbon components (from C27 onwards), condensation/evaporation is relatively slow due to their lower saturation vapour pressures (Table 1). The concentrations of these SVOCs in both gas and particle phases are more dependent on the strength of both emissions and background. As the gas emission fluxes are relatively smaller than particle, their gas-phase concentrations increase slightly at the rooftop and then approach background levels after a downwind distance of 100m. The increment due to emission is more significant in particle concentrations of these higher carbon number SVOCs. During the dispersion process, condensation processes may occur due to the very low saturation vapour pressures for some higher carbon components, e.g. C31-C32 (Table 1).

As shown in Figure 3(c), the rooftop generally has the highest concentrations (both mean and fluctuation concentrations) for all SVOCs (the sum of gas and particle phase concentrations) compared with the downwind locations. The SVOC concentrations rapidly decrease at a short travelling distance and then approach the background levels during their neighbourhood-scale dispersion. Because of mass conservation, each $C_{n,\text{gas+particle}}$ should behave like a passive scalar, possessing the spatial patterns similar to total UFP number concentration shown in Figure 1, with their own background concentration and peak concentration level near the line source. Figure 3(d) illustrates the dilution ratio of SVOC gas and particle phases (defined in the same way as that for UFP number concentrations in Figure 2(b)) for the downwind locations (rooftop+100m and rooftop+400m). For both lower carbon gas-phase components (C16-C20) and higher carbon particle-phase components (C27-C32), the dilution ratio closely follows that of a passive scalar (as indicated by dashed lines, which are also the same as that in Figure 2(b)), indicating that dilution dominates during their neighbourhood dispersion.

For C21-C26, there are variations of dilution ratios along the dashed lines (for a passive scalar) indicating that aerosol condensation/evaporation plays an important role during the neighbourhood scale dispersion. Their gas-phase mass concentrations are reduced more slowly than the rate for a passive scalar (the dilution ratios are above the dashed lines) and their particle-phase mass concentrations are reduced faster than the rate for a passive scalar (the dilution ratios are below the dashed lines).

In summary, the above discussions suggest that the evaporation of low-carbon components (C16-C20) of emitted particles is almost complete on the timescale of less than a second (Table S4 in the Supplementary Material), and this leads to very high C_{gas} and negligible $C_{particle}$ at the rooftop (Figs 3(a) and 3(b)). From the rooftop location to the downwind locations of 100m and 400 m (or travelling

time of about 50 s and 200 s), C_{gas} for C16-C20 follows the dilution rate of a passive scalar (Figure 3(d)). However, the evaporation of the medium-carbon components (C21-C26) of emitted particles is slower, taking the timescale of travelling from the rooftop to 100-400 m downwind (about 50 s and 200 s). This evaporation process converts some medium-carbon component SVOCs from the particle phase to gas phase while the advection-dilution processes are underway during the period (Figure 3(d)). Finally the evaporation (or condensation) of high-carbon components (C27-C32) of emitted particles is extremely slow and within the timescale of travelling, $C_{particle}$ behaves like the dilution of a passive scalar (Figure 3(d)).

3.2 Linearity Analysis Among Cases from the model

To provide insight into the relationships among multiple processes, the linearity of the dependence of several UFP quantities (UFPNSD, all-size particle mass concentration, gas mass concentration, and total mass concentration) on the emission rate and on the inlet background concentration, has been investigated. For this purpose, a scaled concentration for the *ic*th case is defined as follows:

$$\hat{C}^{ic} = (C^{ic} - \alpha C_{bg}^{BASE})/\beta, \quad (7)$$

where C^{ic} is the concentration of any quantity in the *ic*th case, C_{bg}^{BASE} is the background concentration in Case BASE, α and β are the multiplied coefficients for inlet background and emission, respectively (defined in Sect. 2.3). If the linearity is perfect, the profile for any tested case (with the background subtracted) will scale exactly with total emission flux; in other words, the curves of scaled concentrations ($\hat{C}^{ic}$) for all tested cases should collapse into a single curve. Variations in the curves of scaled concentrations, $\hat{C}^{ic}$, would indicate nonlinear behaviour of the UFP system. This test determines whether a reduced microphysical model can be adopted or not: for perfectly scaled behaviour, results for one case can be used to construct the solutions for any multiplication of the emission profile and/or the background concentration profile.

Figure 4 demonstrates the perfect scalability for the spatially and temporally averaged total UFPNC along a South-North line at the bottom level of the domain in the model. All the tested cases, with varying either α or β, collapse onto a single curve, indicating an excellent scalability for total UFPNC. This implies that if the results of a base case are known, the results for any other cases (corresponding to a pair of α and β) can be obtained simply from the scaled equation (Equation 7), i.e. $\hat{C}^{ic} = \beta\hat{C}^{BASE} + \alpha C_{bg}^{BASE}$.

For the rooftop location, there is weak non-linearity (not shown here) as the UFPNSDs are predominately affected by emissions on a very short time scale (only influenced by lower carbon components). Stronger non-linearity, for the downwind location of rooftop+400 m (travelling time of about 200 s), is presented in Figure 5(a). The number concentrations for particles with diameters higher than 100 nm exhibit a very good scalability. This is due to the large mass fraction of non-volatile core in this size range, reducing the effects of evaporation/condensation, so that the behaviour for these particles is very similar to that of passive scalars. For smaller particles, number concentrations are not perfectly scaled. This is due to the nonlinear evaporation process for smaller particles and the change of their particle sizes. If the scaled model (Equation 7) is used to generate an approximate solution, then there would be an error for a non-perfectly scaled quantity (e.g. number concentrations for smaller size bins). For the value range of α and β tested here, the errors are not remarkably large, as illustrated in Fig 5. In order to reveal the details of the scalability, a correction factor defining the error for the ic^{th} case (ϕ^{ic}) relative to case BASE for the scaled quantity is,

$$\phi^{ic} = (\hat{C}^{ic} - \hat{C}^{BASE})/\hat{C}^{BASE}, \quad (8)$$

Figure 5(b) shows correction factors for selected nonlinear bins at the downwind location of rooftop+400m in cases with varying background and emissions from the model. Correction factors

for selected bins are within 10% in most cases for varying emissions and varying background. Correction factors for bin 3 (with bin bounds of [10.7 nm, 14.6 nm]) are generally bigger than those for bin 7 ([36.6 nm, 49.9 nm]), followed by bin 5 ([19.8 nm, 26.9 nm]). For cases of varying background, bin 3 always has an opposite sign compared to bins 5 and 7. From the discussion associated with Figure 2(b) (the output of the BASE case), it is evident that the number concentration of bin 3 increases with the evaporation from particles of bins 5-9. Furthermore, the discussions associated with Figure 3(d) reveal that the evaporation occurs mainly to C21-C26 for a distance of 100-400m (travelling time of about 50 s and 200 s),. The decreasing trend of ϕ for "BG-bin3" with α (indicator of the background concentrations' magnitude) in Figure 5(b) suggests that higher background SVOC concentrations will suppress the evaporation processes of C21-C26 in bins 5-9, thus reducing particle numbers gained in bin 3. This finding is further supported by the increasing trend of ϕ for "BG-bin7" with α in Figure 5(b), as suppressed evaporation causes fewer particle numbers in bin 7 lost to smaller bins. It is interesting to see the trend of curve for "BG-bin5" is similar to that for "BG-bin7", suggesting the particles of bin 5 also contribute to evaporation which is suppressed by higher background concentrations. This suppression of evaporation, however, is not clearly seen for the "EM" cases in Figure 5(b).

Figure 6 shows the scaled concentrations for both SVOC gas and particle concentrations at the downwind location of rooftop+400m (travelling time of about 200 s) from the model. There are very good scalabilities for lower carbon components (e.g. C16-C22). This may be attributed to their high vapour pressure and fast evaporation processes which would transfer particle SVOC mass to vapour very quickly (Nikolova et al., 2018). Then this would be an effective dilution process for gas concentrations (indicating nearly zero particle concentrations for lower carbon numbers in Figure 6(b)).

From C23-C27, the nonlinearity effect becomes more significant because SVOC vapour pressures decrease with carbon number making evaporation slower. For those SVOCs having a timescale of condensation/evaporation comparable to the dilution timescale, the effects of both condensation/evaporation and neighbourhood dilution are significant, leading to significant nonlinearity.

For higher carbon components (C28-C32), vapour pressures are very small (Table 1) and emission rates are relatively smaller than lower carbon components, so only rather slow condensation/evaporation processes occur. Their nonlinearities are less significant, with the dilution process dominating, and only a slight influence of condensation/evaporation.

The sum of gas and particles (Figure 6(c)) can be scaled well although either gas or particles for higher carbon components cannot be scaled well, indicating the evolving partitioning between gas and particles. Figure 6(d) shows correction factors for a selected nonlinear carbon SVOC (C25) at the downwind location of rooftop+400m in cases with varying background and emissions. These correction factors can be up to around 60% for higher background cases and lower emission cases. A consistent pattern is that, as α (or β) increases, the gas concentration of C25 decreases; in other words, increasing α (or β) will suppress the evaporation of SVOCs on the particles. Correction factors for gas concentrations always have opposite signs, and occur in a certain ratio to those for particle concentrations, indicating that the conversion between gas and particles is conservative (Figure 6(c)). This suggests a relationship of correction factors between gas and particles, i.e. $\phi_{gas}^{ic} / \phi_{particle}^{ic} = -\hat{C}_{particle}^{BASE} / \hat{C}_{gas}^{BASE}$, which can also be inferred from Equations 7-8 assuming the conservation of the sum of gas and particle concentrations ($\hat{C}_{gas}^{ic} + \hat{C}_{particle}^{ic} = \hat{C}_{gas}^{BASE} + \hat{C}_{particle}^{BASE}$). The asymmetric patterns of correction factors between the gas phase and the particle phase in Figure 6(d) are due to the BASE value for gas being lower than that for particles.

4. CONCLUSIONS

Size-dependent multicomponent microphysics of UFPs (involving condensation/evaporation of SVOCs) has been coupled with WRF-LES to simulate the neighbourhood dispersion of UFPs for an idealised line (street) emission. UFPs are horizontally advected downwind into the neighbourhood scale and vertically mixed with urban background air. There is evidence of evaporation effects, which alter the size distribution of UFPs. The lightest SVOCs evaporate within a model time step of 0.2 s, while those in a middle range of carbon numbers (C21-C26) evaporate with a timescale about equal to that of mixing. The dispersion and evolution of UFPs at the neighbourhood-scale are the result of combined effects among emissions, mixing with background and evaporation/condensation.

Among a wide range of timescales for the evaporation/condensation of SVOCs (Table S4 in the Supplementary Material), only those of the same order of magnitude as the travelling time have significant contributions to the non-linear part of the UFP concentration field during the neighbourhood-scale dispersion. There is a very good linearity for total UFPNC, UFPNSD (for UFP diameter greater than 100 nm), concentrations of lower carbon components, and concentrations of the sum of both gas and particles. The linearity is less precisely upheld for the number concentration of smaller particles and concentrations of those carbon components with a timescale comparable to the dilution timescale. For the non-perfectly scaled quantities, a linear model may be adopted to yield an approximate solution with a tolerance of an error. For the value range of α and β tested in this study, the errors are about 10% or less for the nucleation mode of particle number concentrations, but can be as large as around 60% for the mass concentrations of medium-carbon SVOC components.

The WRF-LES-UFP model developed in this study reveals the evolution and dispersion of sized-resolved UFPs from an urban street to its neighbourhood-scale surroundings and can be extended straightforwardly to simulate the neighbourhood scale dispersion of UFPs for a realistic street canyon network. Gridded surface emissions based on the real-time traffic reactivity can be implemented as

584 an input in the model to represent a real-world street network. Planned future modelling work is to
585 configure the model with a realistic street canyon network emission pattern and to conduct sensitivity
586 tests of key parameters under different atmospheric conditions.
587
588 **ACKNOWLEDGEMENTS**
589 This work is part of the FASTER project, ERC-2012-AdG, Proposal No. 320821 sponsored by the
590 European Research Council (ERC). JZ, XC, and ARMK gratefully acknowledge additional support
591 from the UK Natural Environment Research Council (NERC: NE/N003195/1 (JZ, XC, ARMK) and
592 NE/S013814/1 (XC, ARMK). The authors appreciate the regional HPC Midlands+ service
593 (http://www.hpc-midlands-plus.ac.uk/) and the University of Birmingham's BlueBEAR HPC service
594 (http://www.bear.bham.ac.uk) for providing the computational resources.
595
596 **CODE AVAILABILITY**
597 WRF v3.6.1 is available at http://www2.mmm.ucar.edu/wrf/users/download/get_sources.html. The
598 coupling WRF v3.6.1 large eddy simulation code with UFP microphysics module and case settings
599 are archived on Zenodo (https://doi.org/10.5281/zenodo.3333811).
600 **DATA AVAILABILITY**
601 Data supporting this publication are openly available from the UBIRA eData repository at
602 https://doi.org/10.25500/edata.bham.00000366
603
604

REFERENCES

Ackermann, I.J., Hass, H., Memmesheimer, M., Ebel, A., Binkowski, F.S., Shankar, U., 1998. Modal aerosol dynamics model for Europe: Development and first applications. Atmos. Environ., 32, 2981-2999, 10.1016/s1352-2310(98)00006-5.

Alam, M.S., Zeraati-Rezaei, S., Stark, C.P., Liang, Z.R., Xu, H.M., and Harrison, R.M., 2016. The characterisation of diesel exhaust particles - composition, size distribution and partitioning. Faraday Discuss., 189, 69-84, 10.1039/c5fd00185d,.

Alam, M.S., Nikolova, I., Singh, A., MacKenzie, A.R., Harrison, R.M., 2019. Experimental vapour pressures of eight n-alkanes (C_{17}, C_{18}, C_{20}, C_{22}, C_{24}, C_{26}, C_{28} and C_{31}) at ambient temperatures. Atmos. Environ., 213, 739-745.

Archer-Nicholls, S., Lowe, D., Darbyshire, E., Morgan, W.T., Bela, M.M., Pereira, G., Trembath, J., Kaiser, J.W., Longo, K.M., Freitas, S.R., Coe, H., McFiggans, G., 2015. Characterising Brazilian biomass burning emissions using WRF-Chem with MOSAIC sectional aerosol. Geosci. Model Dev., 8, 549-577, 10.5194/gmd-8-549-2015.

Baik, J.-J., Kang, Y.-S., Kim, J.-J., 2007. Modeling reactive pollutant dispersion in an urban street canyon. Atmos. Environ., 41, 934-949, 10.1016/j.atmosenv.2006.09.018.

Baldauf, R.W., Devlin, R.B., Gehr, P., Giannelli, R., Hassett-Sipple, B., Jung, H., Martini, G., McDonald, J., Sacks, J.D., Walker, K., 2016. Ultrafine Particle Metrics and Research Considerations: Review of the 2015 UFP Workshop. Int. J. Environ. Res. Public Health, 13, 10.3390/ijerph13111054.

Britter, R. E., Hanna, S. R., 2003. Flow and dispersion in urban areas. Annu. Rev. Fluid Mech., 35, 469-496, 10.1146/annurev.fluid.35.101101.161147.

Carpentieri, M., Salizzoni, P., Robins, A., Soulhac, L., 2012. Evaluation of a neighbourhood scale, street network dispersion model through comparison with wind tunnel data. Environ. Modell. Softw., 37, 110-124, 10.1016/j.envsoft.2012.03.009.

Chin, M., Rood, R.B., Lin, S.-J., Müller, J.-F., and Thompson, A.M., 2000. Atmospheric sulfur cycle simulated in the global model GOCART: Model description and global properties. J. Geophys. Res.: Atmospheres, 105, 24671-24687, 10.1029/2000jd900384.

Compernolle, S., Ceulemans, K., Muller, J.F., 2011. Evaporation: a new vapour pressure estimation methodfor organic molecules including non-additivity and intramolecular interactions. Atmos. Chem. Phys., 11, 9431-9450, 10.5194/acp-11-9431-2011.

Dall'Osto, M., Thorpe, A., Beddows, D.C.S., Harrison, R.M., Barlow, J.F., Dunbar, T., Williams, P. I., Coe, H., 2011. Remarkable dynamics of nanoparticles in the urban atmosphere. Atmos. Chem. Phys., 11, 6623-6637, 10.5194/acp-11-6623-2011.

European Commission: Air Quality Standards. 2017. http://ec.europa.eu/environment/air/quality/standards.htm, 10.1016/s1352-2310(01)00438-1.

Geiser, M., Rothen-Rutishauser, B., Kapp, N., Schurch, S., Kreyling, W., Schulz, H., Semmler, M., Hof, V.I., Heyder, J., Gehr, P., 2005. Ultrafine particles cross cellular membranes by nonphagocytic mechanisms in lungs and in cultured cells. Environ. Health Perspect., 113, 1555-1560, 10.1289/ehp.8006.

Gelbard, F. & Seinfeld, J. H. 1980. Simulation of multicomponent aerosol dynamics. Journal of Colloid and Interface Science, 78, 485-501, 10.1016/0021-9797(80)90587-1.

Grell, G.A., Peckham, S.E., Schmitz, R., McKeen, S.A., Frost, G., Skamarock, W. C., Eder, B., 2005. Fully coupled "online" chemistry within the WRF model. Atmos. Environ., 39, 6957-6975, 10.1016/j.atmosenv.2005.04.027.

Harrison, R.M., Shi, J.P., Xi, S.H., Khan, A., Mark, D., Kinnersley, R., Yin, J. X., 2000. Measurement of number, mass and size distribution of particles in the atmosphere. Philos. T. R. Soc. A, 358, 2567-2579.

Harrison, R.M., Beddows, D.C.S., Dall'Osto, M., 2011. PMF analysis of wide-range particle size spectra collected on a major highway. Environ. Sci.Technol., 45, 5522-5528, 10.1021/es2006622.

Harrison, R.M., Jones, A.M., Beddows, D.C.S., Dall'Osto, M., Nikolova, I., 2016. Evaporation of traffic-generated nanoparticles during advection from source. Atmos. Environ., 125, 1-7, 10.1016/j.atmosenv.2015.10.077.

Harrison, R.M., MacKenzie, A.R., Xu, H.M., Mohammed, S.A., 2018. Diesel exhaust nanoparticles and their behaviour in the atmosphere. Roy. Soc. Proceed. A, 474, 1-20, 10.1016/s1001-6058(08)60125-0.

Harrison, R.M., Beddows, D.C.S., Alam, M.S., Singh, A., Brean, J., Xu, R., Kotthaus, S., Grimmond, S., 2019. Interpretation of particle number size distributions measured across an urban area during the FASTER campaign. Atmos. Chem.Phys., 19, 39-55, 10.5194/acp-19-39-2019.

Jacobson, M.Z., Seinfeld, J.H., 2004. Evolution of nanoparticle size and mixing state near the point of emission. Atmos. Environ., 38, 1839-1850, 10.1016/j.atmosenv.2004.01.014.

Jacobson, M. Z., et al.,1996. Simulating equilibrium within aerosols and nonequilibrium between gases and aerosols. Journal of Geophysical Research-Atmospheres,101,9079-9091, 10.1029/96JD00348.

Jacobson, M. Z. and R. P. Turco,1995. Simulating Condensational Growth, Evaporation, and Coagulation of Aerosols Using a Combined Moving and Stationary Size Grid. Aerosol Science and Technology, 22, 73-92, 10.1080/02786829408959729.

Jacobson, M.Z., 2005. Fundamentals of Atmospheric Modeling, Second Edition ed., Cambridge University Press, New York.

Jacobson, M. Z., Kittelson, D.B., Watts, W.F., 2005. Enhanced coagulation due to evaporation and its effect on nanoparticle evolution. Environ. Sci.Techn., 39, 9486-9492, 10.1021/es0500299.

Jones, A.M., Harrison, R.M., 2006. Estimation of the emission factors of particle number and mass fractions from traffic at a site where mean vehicle speeds vary over short distances. Atmos. Environ., 40, 7125-7137, 10.1016/j.atmosenv.2006.06.030.

Kuik, F., Lauer, A., Churkina, G., Denier van der Gon, H.A.C., Fenner, D., Mar, K. A., Butler, T. M., 2016. Air quality modelling in the Berlin–Brandenburg region using WRF-Chem v3.7.1: sensitivity to resolution of model grid and input data. Geosci. Model Dev., 9, 4339-4363, 10.5194/gmd-9-4339-2016.

Kumar, P., Morawska, L., Birmili, W., Paasonen, P., Hu, M., Kulmala, M., Harrison, R.M., Norford, L., Britter, R., 2014. Ultrafine particles in cities. Environ. Int., 66, 1-10, 10.1016/j.envint.2014.01.013.

Kwak, K. H., Baik, J.J., 2014. Diurnal variation of NO_x and ozone exchange between a street canyon and the overlying air. Atmos. Environ., 86, 120-128, 10.1016/j.atmosenv.2013.12.029.

LeGrand, S. L., Polashenski, C., Letcher, T. W., Creighton, G. A., Peckham, S. E., Cetola, J. D., 2019. The AFWA dust emission scheme for the GOCART aerosol model in WRF-Chem v3.8.1. Geosci. Model Dev., 12, 131-166, 10.5194/gmd-12-131-2019.

Manigrasso, M., Natale, C., Vitali, M., Protano, C., Avino, P., 2017. Pedestrians in traffic environments: Ultrafine particle respiratory doses. Int. J. Environ. Res. Public Health, 14, 10.3390/ijerph14030288.

McHugh, C.A., Carruthers, D.J., Edmunds, H.A., 1997. ADMS-Urban: an air quality management system for traffic, domestic and industrial pollution. Int. J. Environ. Pollut., 8, 666-674.

Moeng, C.H., Dudhia, J., Klemp, J., Sullivan, P., 2007. Examining two-way grid nesting for large eddy simulation of the PBL using the WRF model. Mon. Weather Rev., 135, 2295-2311, 10.1175/mwr3406.1.

Munir, S., Habeebullah, T. M., 2015. Vehicular emissions on main roads in Makkah, Saudi Arabiaa dispersion modelling study. Arab. J.Geosci., 11, 10.1007/s12517-018-3857-z, 2018.

Munoz-Esparza, D., Kosovic, B., van Beeck, J., Mirocha, J., 2015. A stochastic perturbation method to generate inflow turbulence in large-eddy simulation models: Application to neutrally stratified atmospheric boundary layers. Phys. Fluids, 27, 10.1063/1.4913572.

Nikolova, I., MacKenzie, A. R., Cai, X. M., Alam, M. S., Harrison, R. M., 2016. Modelling component evaporation and composition change of traffic-induced ultrafine particles during travel from street canyon to urban background. Faraday Discuss., 189, 529-546, 10.1039/c5fd00164a.

Nikolova, I., Cai, X., Alam, M.S., Zeraati-Rezaei, S., Zhong, J., MacKenzie, A. R., Harrison, R. M., 2018. The influence of particle composition upon the evolution of urban ultrafine diesel particles on the neighbourhood scale. Atmos. Chem. Phys. Discuss., 18, 1-39, 10.5194/acp-2017-1018.

Nottrott, A., Kleissl, J., and Keeling, R.: Modeling passive scalar dispersion in the atmospheric boundary layer with WRF large-eddy simulation, Atmospheric Environment, 82, 172-182, 10.1016/j.atmosenv.2013.10.026, 2014.

Nunalee, C. G., Kosovic, B., and Bieringer, P. E.: Eulerian dispersion modeling with WRF-LES of plume impingement in neutrally and stably stratified turbulent boundary layers, Atmospheric Environment, 99, 571-581, 10.1016/j.atmosenv.2014.09.070, 2014.

Panis, L. I., de Geus, B., Vandenbulcke, G., Willems, H., Degraeuwe, B., Bleux, N., Mishra, V., Thomas, I., and Meeusen, R.: Exposure to particulate matter in traffic: A comparison of cyclists and car passengers, Atmospheric Environment, 44, 2263-2270, 10.1016/j.atmosenv.2010.04.028, 2010.

Pankow, J. F.: An absorption model of gas/particle partitioning of organic compounds in the atmosphere, Atmospheric Environment, 28, 185-188, 10.1016/1352-2310(94)90093-0, 1994.

Popoola, O. A. M., Carruthers, D., Lad, C., Bright, V. B., Mead, M. I., Stettler, M. E. J., Saffell, J. R., and Jons, R. L.: Use of networks of low cost air quality sensors to quantify air quality in urban settings, Atmospheric Environment, 194, 58-70, 10.1016/j.atmosenv.2018.09.030, 2018.

Pugh, T. A. M., Cain, M., Methven, J., Wild, O., Arnold, S. R., Real, E., Law, K. S., Emmerson, K. M., Owen, S. M., Pyle, J. A., Hewitt, C. N., and MacKenzie, A. R.: A Lagrangian model of air-mass photochemistry and mixing using a trajectory ensemble: the Cambridge Tropospheric Trajectory model of Chemistry And Transport (CiTTyCAT) version 4.2, Geoscientific Model Development, 5, 193-221, 10.5194/gmd-5-193-2012, 2012.

Schell, B., Ackermann, I. J., Hass, H., Binkowski, F. S., and Ebel, A.: Modeling the formation of secondary organic aerosol within a comprehensive air quality model system, Journal of Geophysical Research-Atmospheres, 106, 28275-28293, 10.1029/2001jd000384, 2001.

Skamarock, W. C., and Klemp, J. B.: A time-split nonhydrostatic atmospheric model for weather research and forecasting applications, Journal of Computational Physics, 227, 3465-3485, 10.1016/j.jcp.2007.01.037, 2008.

Topping, D., Barley, M., Bane, M. K., Higham, N., Aumont, B., Dingle, N., and McFiggans, G.: UManSysProp v1.0: an online and open-source facility for molecular property prediction and atmospheric aerosol calculations, Geoscientific Model Development, 9, 899-914, 10.5194/gmd-9-899-2016, 2016.

US EPA: NAAQS Table, https://www.epa.gov/criteria-air-pollutants/naaqs-table, 10.1016/s1352-2310(01)00438-1, 2017.

Vu, T. V., Zauli-Sajani, S., Poluzzi, V., Delgado-Saborit, J. M., and Harrison, R. M.: Loss processes affecting submicrometer particles in a house heavily affected by road traffic emissions, Aerosol Science and Technology, 51, 1201-1211, 10.1080/02786826.2017.1343453, 2017.

Zaveri, R. A., Easter, R. C., Fast, J. D., and Peters, L. K.: Model for Simulating Aerosol Interactions and Chemistry (MOSAIC), Journal of Geophysical Research: Atmospheres, 113, 10.1029/2007jd008782, 2008.

Zhong, J., Nikolova, I., Cai, X., MacKenzie, A. R., and Harrison, R. M.: Modelling traffic-induced multicomponent ultrafine particles in urban street canyon compartments: Factors that inhibit mixing, Environmental Pollution, 238, 186-195, https://doi.org/10.1016/j.envpol.2018.03.002, 2018.

TABLE LEGEND:

Table 1. Initial/background partial pressure (derived from vapour concentrations on a urban background site) and saturation vapour pressures estimated at temperature of 284.15 K based on the UManSysProp online tool using data from Compernolle et al. (2011).

FIGURE LEGENDS:

Figure 1. Total UFP number concentration (# cm^{-3}): Vertical slice of (a) mean concentration (C_m) and (b) the ratio of concentration fluctuation intensity to mean concentration (C'/C_m); (c) mean concentration with fluctuations along South-North line (starting from 200 m before the emission) at the bottom level.

Figure 2. (a) UFP number-size distribution dN/dlogDp (# cm^{-3}) (fluctuation intensity indicated by shaded areas) for rooftop and its downwind neighbourhood at the bottom level; The inflowing background is taken from 200 m before the emission at the bottom level of the domain;The size-dependent emission flux $dE/dlogD_p$ is shown for comparison. (b) Dilution ratio for the downwind locations; Dashed lines represent the dilution ratio for a passive-like scalar (e.g. total UFP number concentration) at each downwind locations. Rooftop +100 m and +400 m represent the travelling time of about 50 m and 200 s, respectively, in this study.

Figure 3. SVOCs concentration (ng m^{-3}) (fluctuation information indicated by shaded areas) at the rooftop and its downwind neighbourhood locations at the bottom level: (a) Gas concentrations; (b) Particle concentrations, (c) Sum of gas and particle concentrations and (d) Dilution ratio for the downwind locations (The absolute concentrations for high-carbon gas-phase components and for low-carbon particle-phase components are very close to the background concentrations; therefore the dilution ratios for these components are not shown.); Dash lines represent the dilution ratio for a passive-like scalar (also indicated in Figure 4b) at each downwind locations. Rooftop +100 m and +400 m represent the travelling time of about 50 m and 200 s, respectively, in this study.

Figure 4. Scaled total UFP number concentration along South-North line at the bottom level.

Figure 5. (a) Scaled UFP number-size distributions and (b) ϕ for selected bins (bins 3, 5 and 7 with bin bounds of [10.7 nm, 14.6 nm], [19.8 nm, 26.9 nm] and [36.6 nm, 49.9 nm], respectively) at rooftop+400m (or travelling time of about 200 s) for the bottom level.

Figure 6. Scaled SVOC (a) gas concentrations, (b) particle concentrations, (c) the sum of both gas and particle concentrations and (d) Correction factor for a typical SVOC C25 for rooftop+400m (or travelling time of about 200 s) at the bottom level.

Table 1. Initial/background partial pressure (derived from vapour concentrations on an urban background site) and saturation vapour pressures estimated at temperature of 284.15 K based on the UManSysProp online tool using data from Compernolle et al. (2011).

N-alkanes	Partial pressure (in Pa)	Saturation vapour pressure at 284.15 K (in Pa)
C16	1.19E-007	6.42E-02
C17	8.90E-008	1.91E-02
C18	4.44E-008	5.69E-03
C19	2.77E-008	1.70E-03
C20	1.20E-008	5.05E-04
C21	4.16E-009	1.50E-04
C22	1.29E-008	4.48E-05
C23	1.73E-008	1.33E-05
C24	2.29E-008	3.97E-06
C25	1.76E-008	1.18E-06
C26	8.74E-009	3.52E-07
C27	5.73E-009	1.05E-07
C28	5.80E-009	3.12E-08
C29	3.57E-009	9.30E-09
C30	2.73E-009	2.77E-09
C31	4.46E-009	8.25E-10
C32	4.31E-009	2.46E-10

(a) C_m **(# cm^{-3})**

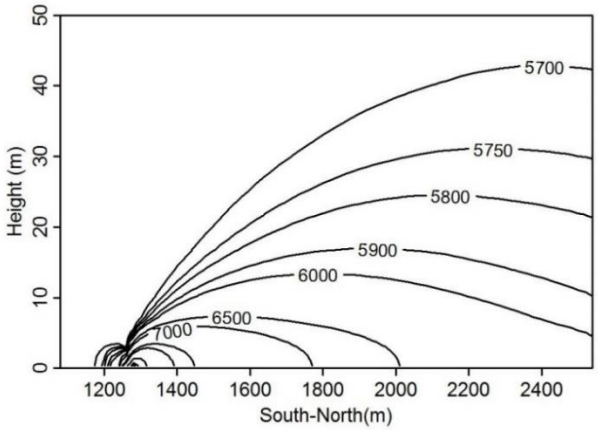

(b) C'/C_m

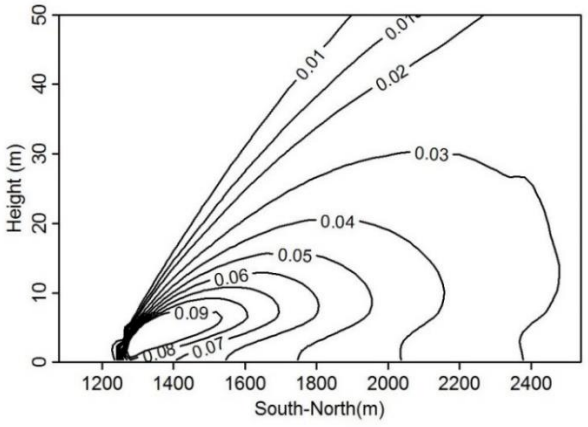

(c) $C_m \pm C'$along the South-North line

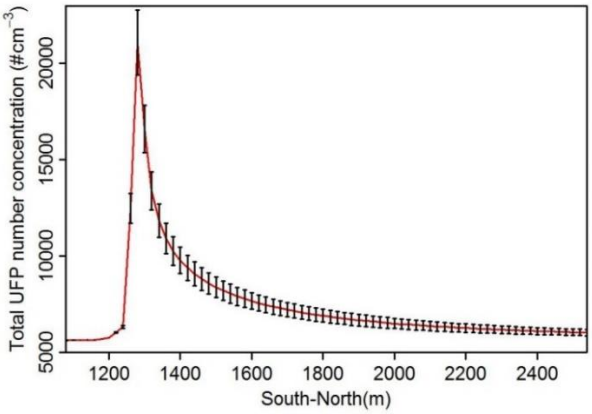

Figure 1. Total UFP number concentration (# cm^{-3}): Vertical slice of (a) mean concentration (C_m) and (b) the ratio of concentration fluctuation intensity to mean concentration (C'/C_m); (c) mean concentration with fluctuations along South-North line (starting from 200 m before the emission) at the bottom level from the model.

(a) **(b)**

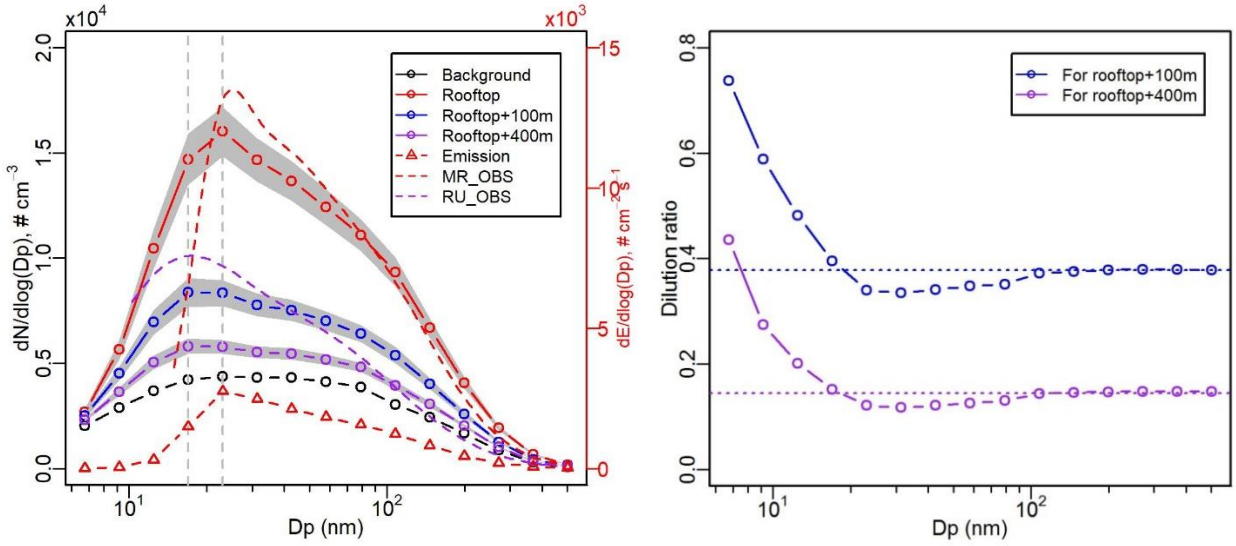

Figure 2. (a) UFP number-size distribution dN/dlogDp (# cm^{-3}) (fluctuation intensity indicated by shaded areas) for rooftop and its downwind neighbourhood at the bottom level; The inflowing background is taken from 200 m before the emission at the bottom level of the domain; The size-dependent emission flux $dE/dlogD_p$ is shown for comparison; MR_OBS represents the measurement from Marylebone roadside; RU_OBS represents the measurement from the nearby downwind rooftop location. (b) Dilution ratio for the downwind locations; Dashed lines represent the dilution ratio for a passive-like scalar (e.g. total UFP number concentration) at each downwind locations. Rooftop +100 m and +400 m represent the travelling time of about 50 m and 200 s, respectively, in this modelling study.

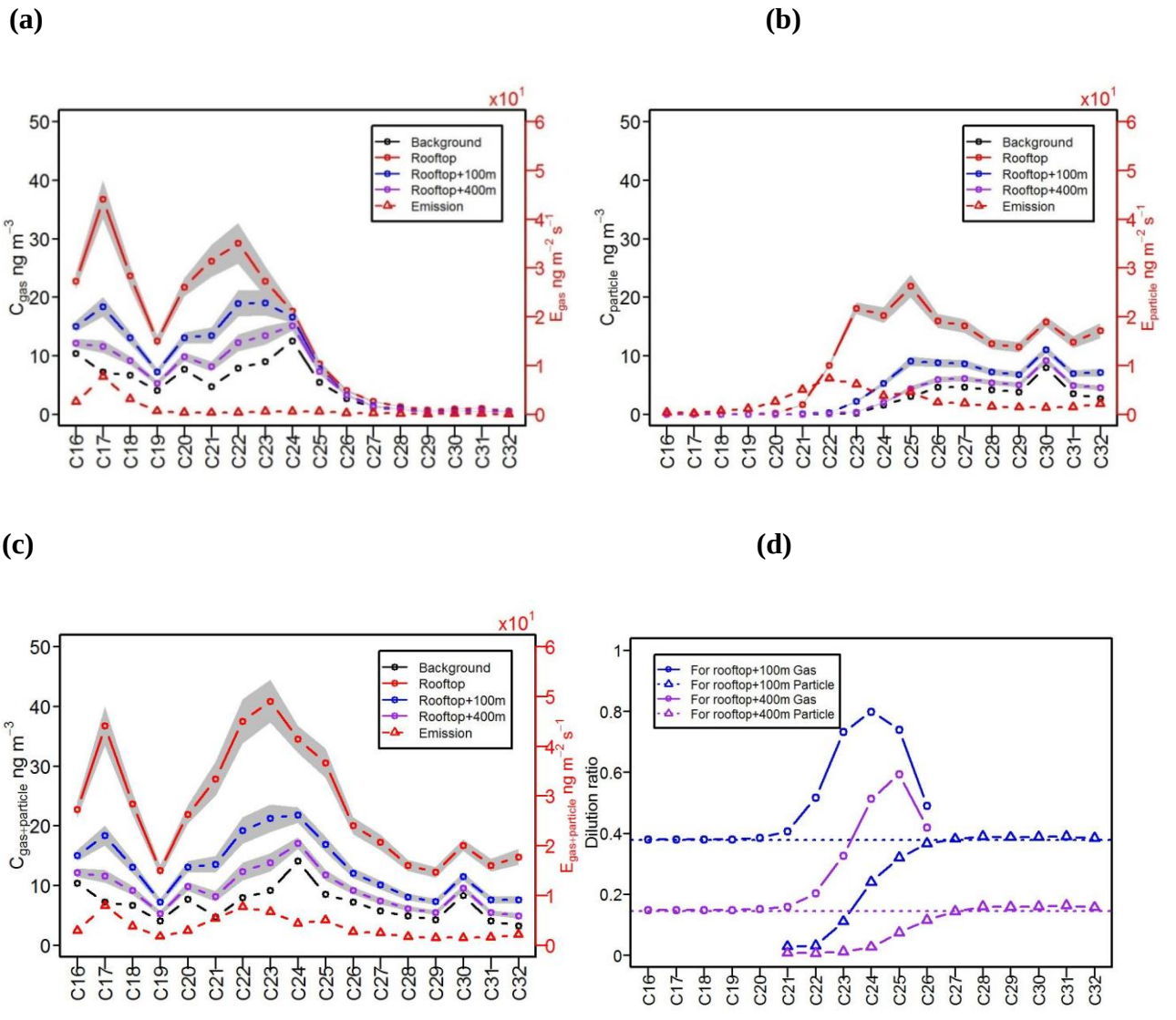

Figure 3. SVOCs concentration (ng m^{-3}) (fluctuation information indicated by shaded areas) at the rooftop and its downwind neighbourhood locations at the bottom level: (a) Gas concentrations; (b) Particle concentrations, (c) Sum of gas and particle concentrations and (d) Dilution ratio for the downwind locations (The absolute concentrations for high-carbon gas-phase components and for low-carbon particle-phase components are very close to the background concentrations; therefore the dilution ratios for these components are not shown.); Dash lines represent the dilution ratio for a passive-like scalar (also indicated in Figure 4b) at each downwind locations. Rooftop +100 m and +400 m represent the travelling time of about 50 m and 200 s, respectively, in this modelling study.

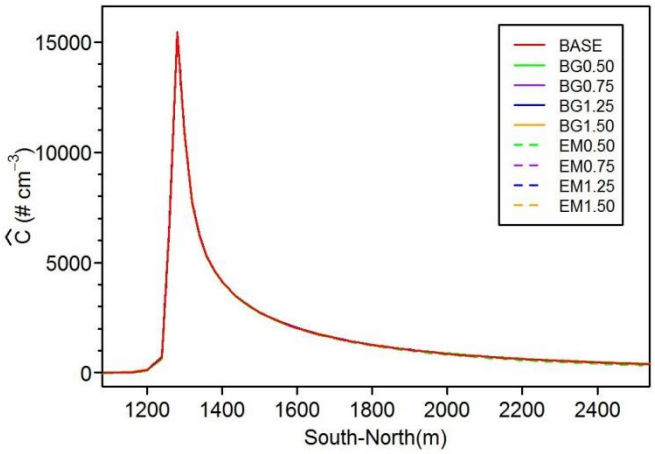

885

886 **Figure 4.** Scaled total UFP number concentration along South-North line at the bottom level from
887 the model.

888

889

890 **(a)** $d\widehat{N}/dlog(Dp)$ **at rooftop+400m** **(b)** ϕ **for selected bins at rooftop+400m**

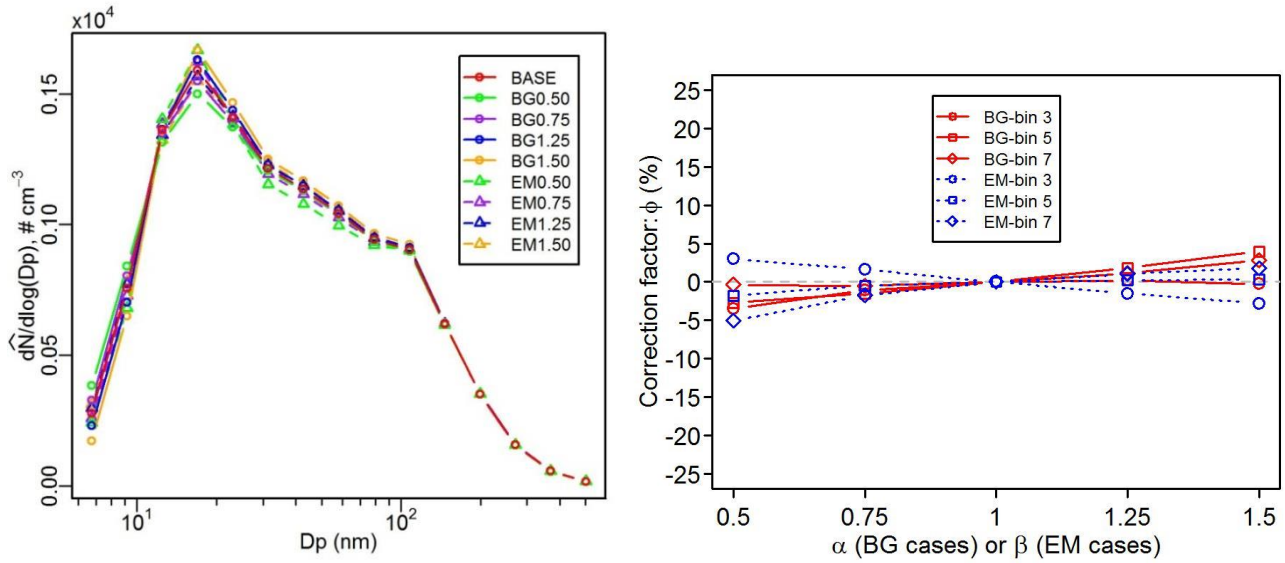

891

892 **Figure 5.** (a) Scaled UFP number-size distributions and (b) ϕ for selected bins (bins 3, 5 and 7 with
893 bin bounds of [10.7 nm, 14.6 nm], [19.8 nm, 26.9 nm] and [36.6 nm, 49.9 nm], respectively) at
894 rooftop+400m (or travelling time of about 200 s) for the bottom level from the model.

895

(a) $\hat{C}_{gas}$ **at rooftop+400m**

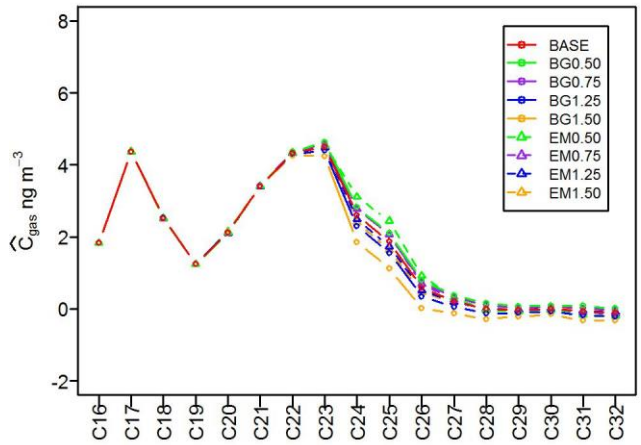

(b) $\hat{C}_{particle}$ **at rooftop+400m**

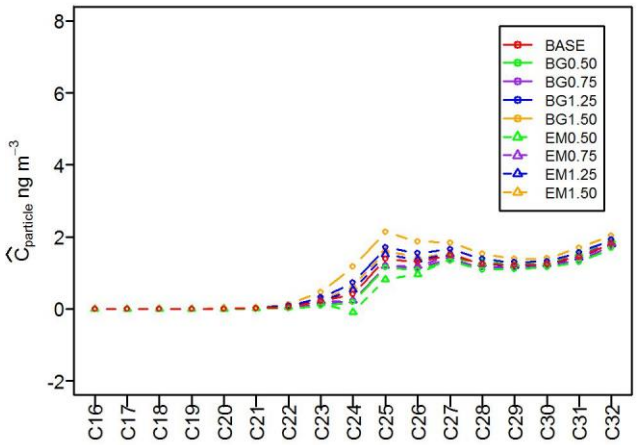

(c) $\hat{C}_{gas+particle}$ **at rooftop+400m**

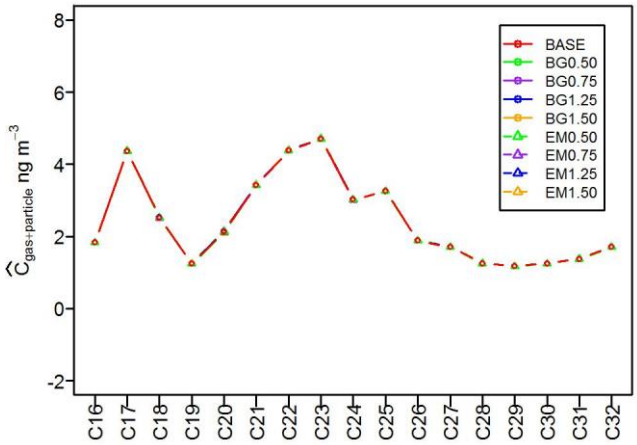

(d) ϕ **for C25 at rooftop+400m**

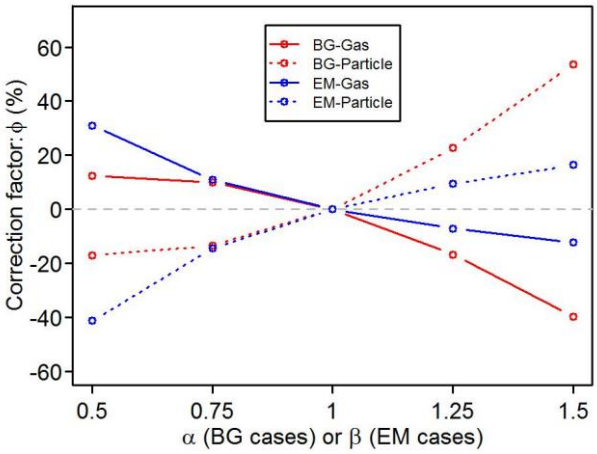

Figure 6. Scaled SVOC (a) gas concentrations, (b) particle concentrations, (c) the sum of both gas and particle concentrations and (d) Correction factor for a typical SVOC C25 for rooftop+400m (or travelling time of about 200 s) at the bottom level from the model.